Available online at www.sciencedirect.com
ScienceDirect
International Journal of Solids and Structures 45 (2008) 2024–2041
INTERNATIONAL JOURNAL OF SOLIDS AND STRUCTURES
www.elsevier.com/locate/ijsolstr

Effect of geometry upon the performance of a thin film ferroelectric capacitor

I. Pane [a,*], N.A. Fleck [b], J.E. Huber [c], D.P. Chu [b,d]

[a] Department of Civil Engineering, Bandung Institute of Technology, Ganesha 10, Bandung 40132, Indonesia
[b] Department of Engineering, University of Cambridge, Trumpington Street CB2 1PZ, UK
[c] Department of Engineering Science, University of Oxford, Parks Road OX1 3PJ, UK
[d] Cambridge Research Laboratory of Epson, 9a Science Park CB4 0FE, UK

Received 5 June 2007; received in revised form 8 November 2007
Available online 8 December 2007

Abstract

The finite element method is used to investigate the performance of a ferroelectric random access memory as a function of its geometry. Performance is characterised by the charge versus electric field relation, and the sensitivity of performance to geometry is explored. The primary geometric variables are the dimensions of a prismatic two-dimensional (2D) island of ferroelectric material, and the edge inclination angle caused by the etching process along the sides of the island. The performance of the two-dimensional ferroelectric device is compared to those of an unsupported ferroelectric thin film and of a ferroelectric film bonded to a substrate.

Keywords: Ferroelectric; Film; Memory; PZT; Substrate

1. Introduction

The electromechanical behaviour of ferroelectrics is commonly exploited in applications such as actuators, sensors and accelerators where electrical energy and mechanical energy are inter-converted. Ferroelectrics in actuators and sensors are pre-poled and are loaded sufficiently lightly that they display a linear piezoelectric characteristic. In contrast, Ferroelectric Random Access Memory (FeRAM) devices operate in the non-linear range due to polarisation switching. Data storage in a FeRAM device is realised by sequentially polarising the ferroelectric film into one of two opposite polarisation directions. FeRAM is a candidate non-volatile memory for high speed computers: it has the advantages of fast read and write, is highly rewritable, scalable, and is compatible with Si technology—either as a stand-alone chip or embedded within an on-chip system. Because of the huge market potential for non-volatile memory devices, FeRAM has attracted considerable research interest, see for example the review by Scott et al. (2005). The successful development of FeRAM is partially

* Corresponding author.
E-mail address: ivpane@netscape.net (I. Pane).

0020-7683/$ - see front matter © 2007 Elsevier Ltd. All rights reserved.
doi:10.1016/j.ijsolstr.2007.11.017

limited by a lack of understanding for their switching response. Although a substantial research effort has focused on the electrical behaviour of FeRAM devices, there is little detailed work on modelling their electromechanical characteristics.

It is problematic to model the performance of a FeRAM device due to the non-linear nature of the ferroelectric switching event. Switching involves a change in remnant strain, and the presence of a substrate and surrounding passive layer makes switching more difficult and induces deleterious stresses within the device. Furthermore, a FeRAM device commonly comprises a thin film with its sides inclined relative to the substrate. The presence of sharp corners gives rise to singular stress and electric fields and lead to premature breakdown of the device. The main aim of the current study is to explore the role played by device geometry upon its electromechanical performance.

1.1. Review of ferroelectric switching

In perovskite ferroelectrics such as lead zirconia titanate (PZT), each crystal is paraelectric above the Curie temperature T_c, and is ferroelectric below T_c. At temperatures above the Curie temperature, the cubic state is stable and no spontaneous polarisation exists within the unit cell, as shown in Fig. 1a. Upon cooling to below the Curie temperature the unit cell transforms to the tetragonal state (or to the orthorhombic state) with the central cation displaced, to create a net dipole moment known as a polarisation, see Fig. 1b. The direction of

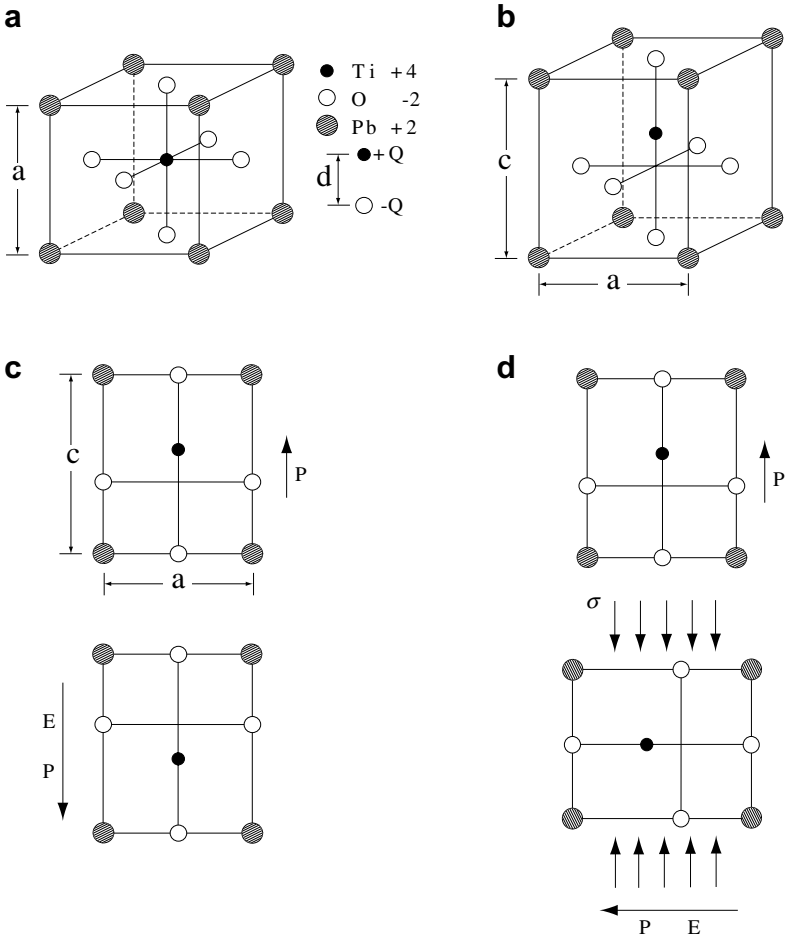

Fig. 1. Unit cell of the provskite structure of PZT-based: (a) Cubic state, (b) tetragonal state, (c) tetragonal state undergoing 180° switching and (d) tetragonal state undergoing 90° switching.

polarisation can be switched by an electric field or by mechanical stress, as illustrated in Fig. 1c and d. The switching (180°) causes a reversal of the polarisation direction with no mechanical distortion of the unit cell, see Fig. 1c. Consequently, this switching event can be triggered by an electric field but not by stress. In contrast, 90° switching produces a change in both the polarisation direction and in the shape of the unit cell; this switching event can be induced either by electric field or by stress. A FeRAM device makes use of mainly 180° switching to store information.

It is recognised that ferroelectric switching involves both the nucleation of new domains and domain wall motion. Rate dependent micromechanical models of ferroelectric switching have been developed recently by Huber and Fleck (2001), Li et al. (2001), Li et al. (2002) and Loge and Suo (1996). Such rate dependence is consistent with observations by Paruch et al. (2005) and Tybell et al. (2002). In this study, we shall make use of a rate dependent crystal plasticity formulation by Huber and Fleck (2001) to model the switching of two-dimensional (2D) ferroelectric islands upon a substrate. It takes into account the relative contributions from the motion of both 90° and 180° domain walls.

1.2. FeRAM device: geometry and principle of operation

A standard ferroelectric capacitor in a FeRAM device is sketched in Fig. 2. It comprises a thin film of ferroelectric of thickness about 100 nm, sandwiched between two electrodes. The bottom electrode is bonded to a silicon substrate while the top electrode is coated by a passivation layer of thickness about 10 μm. During operation, binary information (one bit) is assigned to a bi-polar state of polarisation. For example, "0" is represented by a downward net polarisation within the film, while "1" is represented by an upward polarisation, see Fig. 2. The polarisation direction is switched by applying a voltage pulse to the electrodes, with the pulse duration as short as sub-nanosecond. The stored direction of polarisation is subsequently detected in a number of ways, including charge sensing and electric field effect sensing, see for example Chu (2004).

FeRAM devices are now commercially available and are based mainly upon lead zirconia titanate (PZT) due to its large polarisation. The relation between composition and properties has been comprehensively explored for PZT, see for example Shirane and Hoshino (1951), Jaffe et al. (1954) and Jaffe et al. (1971). Thin film PZT is commonly used for FeRAM mainly because of its large polarisation. In addition, PZT can be processed at a lower temperature than its main competitor strontium bismuth titanate (SBT).

The remnant polarisation of a thin film ferroelectric is less than that of the bulk ferroelectric. This is partly due to mechanical clamping of the thin film by the substrate, and partly due to the microstructure of the thin film relative to that of the bulk. In addition, ferroelectric thin films have a greater coercive field than the bulk material of similar composition. A coercive field of 2.6–8 MV/m and remnant polarisation of 0.01–0.3 C/m^2 have been reported for PZT films regardless of whether they were prepared by a sol–gel technique (Yi et al.,

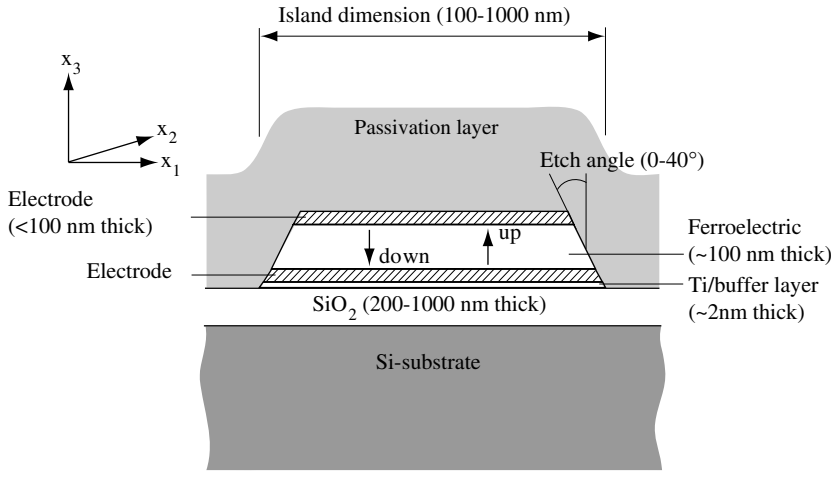

Fig. 2. Typical structure of a ferroelectric capacitor for FeRAM device. The arrows 'up' and 'down' refer to the polarisation directions.

1988; Tang et al., 2003; Kim et al., 2004) or by DC magnetic sputtering technique (Sreenivas and Sayer, 1988). In addition, the coercive field of a thin film scales inversely with its thickness, see the recent review by Dawber et al. (2005) and references therein. The switching characteristics of a FeRAM capacitor also depends upon the absolute size and shape of the device, see Alexe et al. (2001), Alexe et al. (2000) and Jung et al. (2004). All these factors must be considered in designing a thin film FeRAM device.

Numerical models for simulation of the ferroelectric behaviour have undergone rapid development. However, micromechanical simulations have been mainly performed to guide the design of actuators and sensors (Zhang and Bhattacharya, 2005; Gong and Suo, 1996). Some initial attempts have been made to model the electrical performance of a FeRAM capacitor, but these studies have not considered the shape of the device, see for example Li et al. (2001), Li et al. (2002), Pintilie et al. (2005), Pintilie and Alexe (2005) and Miller et al. (1990). The main objective of our work is to simulate the performance of a thin film ferroelectric capacitor used for FeRAM, as influenced by geometry and substrate clamping. The constitutive description is chosen to represent a PZT-based tetragonal ferroelectric.

2. Scope of study

Three discrete problems are considered, all for a thin film ferroelectric of uniform thickness h, see Fig. 3. In all three problems, the film material is a single crystal ferroelectric with the [100] crystal orientation normal to the face of the film and along the x_3-axis, see Fig. 2. The switching response of a ferroelectric free thin film is addressed in problem I, while the same thin film is perfectly bonded to a substrate in problem II. Two types of free film are considered: a free-standing film (Fig. 3a) and a plane strain film, constrained to have zero strain along a single in-plane direction (Fig. 3b). For the bonded film (Fig. 3c), full constraint is applied biaxially to maintain compatibility with the substrate.

In problem III, a finite 2D ferroelectric island, of rectangular cross-section $2w$ by h is bonded to a thick substrate. Both a compliant substrate, with elastic moduli equal to those of the film and a rigid substrate are considered. It is assumed that the passivation layer on top of the device is sufficiently compliant that its presence can be neglected. The electrode layers are of vanishing thickness and their presence is modelled by appropriate boundary conditions: uniform electrical potentials are applied to the top and bottom faces of the ferroelectric film. The effect of the electrode layer, a passivation layer, and other types of substrate upon device performance is beyond the scope of the present work, and is addressed in a subsequent publication. Finite electrode layers and a passivation layer cause some form of restraint to the ferroelectric film. In this study, we intend to investigate the case where restraint provided solely by the substrate. A state of plane strain is assumed for the 2D island, with zero straining and zero electric field in the direction normal to the cross-section of the device. Additionally, for the 2D island, zero charge and traction are assumed along the side edges.

In all three problems, a voltage $\Phi(t)$ is applied to the top electrode while the bottom electrode is grounded. It is assumed that $\Phi(t)$ has a triangular waveform. This voltage induces a uniform electric field of magnitude Φ/h in the free and constrained films. In contrast, the electric field is non-uniform within the 2D island of problem III.

3. Field equations and constitutive law

3.1. Field equations

Mechanical equilibrium of a ferroelectric body demands that

$$\sigma_{ij,j} = 0 \tag{1}$$

where σ_{ij} is the stress and the usual subscript notation is assumed. The small strain tensor ϵ_{ij} is related to the displacement field u_i in the usual manner, $\epsilon_{ij} = (u_{i,j} + u_{j,i})/2$. Unless otherwise stated, repeat suffices imply summations over the relevant dimensions, i.e. $i = 1, 2$ for the 2D case and $i = 1, 2, 3$ for the 3D case. The static electrical field in a ferroelectric body is dictated by Gauss's law relating the divergence of the electric displacement D_i to the free charge density q,

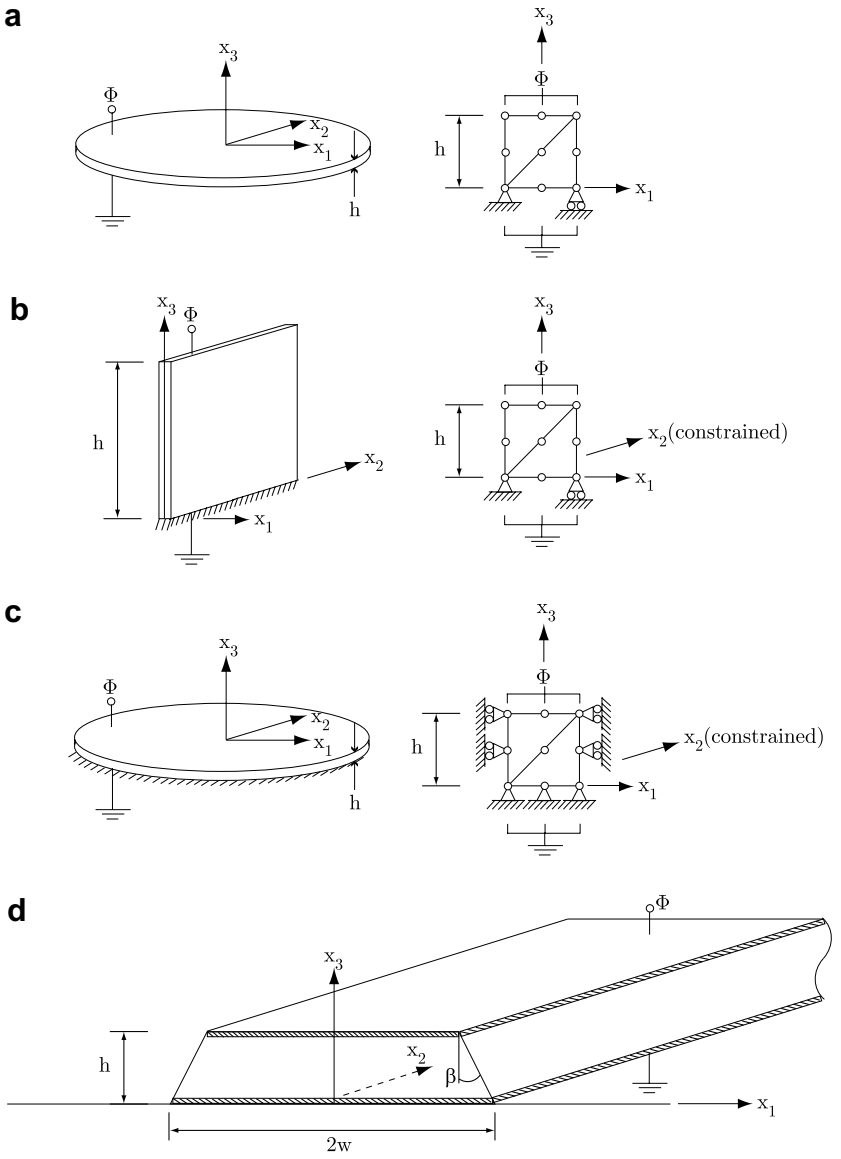

Fig. 3. Geometry and finite element mesh for (a) 1D free-standing film, (b) 1D plane strain film, (c) 1D fully constrained film and (d) 2D finite island.

$$D_{i,i} - q = 0 \tag{2}$$

The electric field E_i is the negative gradient of the electric potential ϕ, according to

$$E_i = -\phi_{,i} \tag{3}$$

On the surface S of the body of unit outward normal n_i, the traction t_i balances the stress σ_{ij} according to

$$t_j = n_i \sigma_{ij} \tag{4}$$

and the charge density Q balances the jump in the electric displacement $[D_i]$ across S such that

$$Q = n_i [D_i] = n_i (D_i^0 - D_i) \tag{5}$$

Here, [ ] denotes the jump in a quantity across the boundary and D_i^0 denotes the electrical displacement exterior to the body.

3.2. Constitutive law

The rate dependent constitutive law is based on that of Huber and Fleck (2001). It is capable of modelling single crystal and polycrystal ferroelectric behaviour. The elastic strain is obtained by subtracting the remnant strain ϵ_{ij}^r, from the total strain ϵ_{ij}. Similarly, the reversible electric displacement is obtained by subtracting the remnant polarisation P_i from the total electric displacement D_i. The elastic strain and the reversible electric displacement depend upon the electric field and stress by the usual linear piezoelectric relations,

$$\epsilon_{ij} - \epsilon_{ij}^r = s_{ijkl}\sigma_{kl} + d_{kij}E_k \tag{6}$$

$$D_i - P_i = d_{ikl}\sigma_{kl} + \kappa_{ik}^{\sigma}E_k \tag{7}$$

where s_{ijkl}, d_{kij} and κ_{ik}^{σ} are, respectively, the elastic compliance tensor, piezoelectric tensor and dielectric permittivity tensor at constant stress. The non-linear switching behaviour enters through the non-linear dependence of ϵ_{ij}^r and P_i upon (σ_{ij}, E_i).

The above piezoelectric relations can be rearranged to a form which is more suitable for displacement and electric potential-based finite element formulation:

$$\sigma_{ij} = c_{ijkl}(\epsilon_{kl} - \epsilon_{kl}^r) - e_{kij}E_k \tag{8}$$

$$D_i = e_{ikl}(\epsilon_{kl} - \epsilon_{kl}^r) + \kappa_{ik}^{\epsilon}E_k + P_i \tag{9}$$

where $e_{kij} = c_{ijmn}d_{kmn}$, $\kappa_{ik}^{\epsilon} = \kappa_{ik}^{\sigma} - d_{irs}c_{pqrs}d_{kpq}$, and c_{ijkl} is the elastic stiffness tensor.

3.2.1. Crystal plasticity model

Domain switching is described by the crystal plasticity theory detailed in Huber et al. (1999) and Huber and Fleck (2001). A brief summary suffices here. The ferroelectric film is treated as a single tetragonal crystal with six variants or domains of mutually orthogonal polarisation, as sketched in Fig. 4. The total number of the switching or transformation systems that can be simultaneously active is 15, but upon treating the reversed switching as independent the total number becomes 30. Each transformation system is denoted by the index α.

It is assumed that the Ith domain has a transversely isotropic piezoelectric tensor:

$$d_{ijk}^I = d_{33}n_in_jn_k + d_{31}(n_i\delta_{jk} - n_in_jn_k) + d_{15}(\delta_{ij}n_k - 2n_in_jn_k + \delta_{ik}n_j) \tag{10}$$

as characterised by the three constants d_{33}, d_{31} and d_{15}. The vector n_i indicates the polarisation direction. Each domain has a volume fraction c_I and is subjected to the same macroscopic uniform stress σ_{ij} and electric field E_i. Both the linear and remnant parts of the strain ϵ_{ij} and of the electric displacement D_i within the ferroelectric solid are given by volume-averages over the crystal. Consequently, the macroscopic piezoelectric tensor of the crystal d_{ijk} equals to $\sum_{I=1}^{M} c_I d_{ijk}^I$, where $M = 6$ is the number of domains. For simplicity, the elastic stiffness c_{ijkl} and dielectric permittivity κ_{ij} of each domain are taken to be isotropic and do not vary from domain to domain. Then, the relations (8) and (9) can be rewritten as:

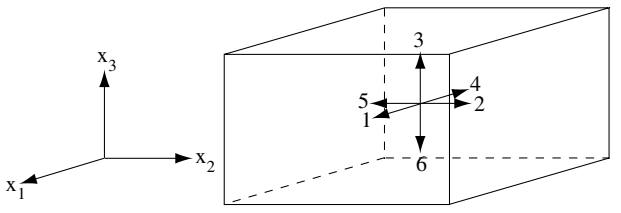

Fig. 4. Coordinate system in a tetragonal ferroelectric crystal, and domain systems 1–6.

$$\sigma_{ij} = c_{ijkl}(\epsilon_{kl} - \epsilon^r_{kl}) - \sum_{I=1}^{M} c_I e^I_{kij} E_k \tag{11}$$

$$D_i = \sum_{I=1}^{M} c_I e^I_{ikl}\left(\epsilon_{kl} - \epsilon^r_{kl}\right) + \kappa^{\epsilon}_{ik} E_k + P_i \tag{12}$$

It is emphasised that the isotropic elasticity tensor c_{ijkl} depends only upon the shear modulus μ and Poisson ratio ν, while the isotropic permittivity tensor scales with a single constant κ. The piezoelectric tensor e^I_{kij} is related to d^I_{ijk} of (10) via $e^I_{kij} = c_{ijmn} d^I_{kmn}$

Full switching of the αth transformation generates a change of remnant strain by $\Delta\epsilon^{r,\alpha}_{ij}$, of remnant polarisation by ΔP^{α}_i, and of the piezoelectric tensor by Δd^{α}_{ijk}. If the Ith domain has a polarisation vector n_i, then its remnant strain is $\epsilon^{r,I}_{ij} = \epsilon_0(3n_i n_j - \delta_{ij})/2$ which gives $\Delta\epsilon^{r,\alpha}_{ij} = \epsilon^{r,I}_{ij} - \epsilon^{r,J}_{ij}$. For a tetragonal lattice with two identical lattice constants a and a larger lattice constant c, the lattice strain is $\epsilon_0 = (c-a)/a$. The change in remnant polarisation ΔP^{α}_i is equal to $s^{\alpha}_i P_0$, where s^{α}_i is a unit vector in the direction of the change in remnant polarisation and P_0 is the maximum polarisation. The change in piezoelectric tensor is given by $\Delta d^{\alpha}_{ijk} = d^I_{ijk} - d^J_{ijk}$. Using these quantities, the driving force for αth transformation G^{α} is defined as:

$$G^{\alpha} = \sigma_{ij}\Delta\epsilon^{r,\alpha}_{ij} + E_i s^{\alpha}_i P_0 + \sigma_{ij}\Delta d^{\alpha}_{kij} E_k \tag{13}$$

Previous studies by Huber et al. (1999) and Kessler and Balke (2001) have identified the physical meaning of G^{α} as the driving force for domain wall motion. In expression (13), terms in Δc^{α}_{ijkl} and $\Delta\kappa^{\sigma\alpha}_{ik}$ are neglected, on the basis that the anisotropy in the elastic and dielectric moduli are relatively small compared to that of the piezoelectric moduli, as discussed by Huber and Fleck (2001).

The rate of change of domain volume fraction for the αth transformation is denoted by a scalar $\dot{f}^{\alpha}$. It depends upon G^{α} normalised by the critical driving force (G^{α}_c) and upon the volume fraction involved in the αth transformation, normalised by the initial fraction (c_0) according to:

$$\dot{f}^{\alpha} = \dot{f}_0 \left|\frac{G^{\alpha}}{G^{\alpha}_c}\right|^{m-1} \frac{G^{\alpha}}{G^{\alpha}_c} \left(\frac{c_I}{c_0}\right)^{1/k} \tag{14}$$

In the above, $\dot{f}_0$ plays the role of a reference rate of switching. With $m \gg 1$, G^{α}_c becomes the critical value of G^{α} at which there is a rapid increase in transformation rate. The volume fraction c_I controls the saturation of transformation system α with sensitivity defined by the exponent k. The state with all $c_I = c_0$ corresponds to an initial, unpoled condition. When $c_I = 0$, the system α is saturated. The rate of change of remnant strain, remnant polarisation, and of the piezoelectric tensor read:

$$\dot{\epsilon}^r_{ij} = \sum_{\alpha=1}^{N} \dot{f}^{\alpha}\Delta\epsilon^{r,\alpha}_{ij} \tag{15}$$

$$\dot{P}_i = \sum_{\alpha=1}^{N} \dot{f}^{\alpha} s_i P_0 \tag{16}$$

$$\dot{d}_{ijk} = \sum_{\alpha=1}^{N} \dot{f}^{\alpha}\Delta d^{\alpha}_{ijk} \tag{17}$$

In the rate independent limit, G^{α}_c is the energy barrier for αth transformation. Its value is determined by considering the one-dimensional case of a free-standing film under uniaxial electrical loading. Assume that the solid has six possible polarisation directions as shown in Fig. 4, with unit normal to the film aligned in the x_3 direction. Relation (13) then gives $G^{180}_c = 2E_{180}P_0$ and $G^{90}_c = \sqrt{2}E_{90}P_0$, where E_{180} and E_{90} are the electric field required for 180° and 90° switching, respectively. The ratio $r = G^{90}_c/G^{180}_c$ then equals $E_{90}/\sqrt{2}E_{180}$.

The initial conditions for any switching event include an initial stress state and the initial volume fraction of ferroelectric domains. In principle, these initial conditions can be found by evaluating the processing route taken to produce the FeRAM device. Here, we limit our scope to a film that is initially in the state of zero residual stress and contains an equal volume fraction of all domains.

The switching characteristic of a memory device will be presented as D_3/P_0 versus the electric field E_3 for the cases of free-standing film, plane strain film and fully constrained film. For the finite 2D ferroelectric island, the averaged surface charge density q_s on each electrode is plotted against Φ/h.

3.3. Finite element implementation

The above constitutive law can be recast in a form suitable for finite element implementation. A standard displacement and electric potential-based FE formulation has been chosen. In the case of a linear piezoelectric constitutive law, the formulation is similar to that of Alik and Hughes (1970). A weak variational statement of the field Eqs. (1)–(5) reads:

$$\int_V [\sigma_{ij}\delta\epsilon_{ij} + D_i\delta E_i]\mathrm{d}V = \int_S [t_i\delta u_i - Q\delta\phi]\mathrm{d}S + \int_V [f_i\delta u_i + q\delta\phi]\mathrm{d}V \tag{18}$$

where V and S denotes, respectively, the volume and the surface of the solid. The variational statement is then rewritten in rate form, and integrated step-by-step by the rate tangent method (see Appendix A) including an equilibrium correction term, to give

$$\Delta t \int_V \left[\dot{\sigma}_{ij}\delta\epsilon_{ij} + \dot{D}_i\delta E_i\right]\mathrm{d}V = \Delta t \int_S \left[\dot{t}_i\delta u_i + \dot{Q}\delta\phi\right]\mathrm{d}S + \left\{\int_S [t_i\delta u_i + Q\delta\phi]\mathrm{d}S - \int_V [\sigma_{ij}\delta\epsilon_{ij} + D_i\delta E_i]\mathrm{d}V\right\} \tag{19}$$

The last term in curly brackets ensures continued equilibrium. The rate tangent method is chosen to improve the numerical stability of the non-linear problem. It has been frequently used in the context of the crystal plasticity modelling of metals (Peirce et al., 1983; Needleman et al., 1985). A similar computational procedure has been used by Haug et al. (2007) for ferroelectrics, where the derivation for the rate tangent method is slightly different from that given here.

The detailed derivation of the above FE procedure is given in Appendix B. This computation has been implemented in Fortran 90. The geometry and element meshing (pre-processing) were generated using ABAQUS (2004). Post-processing was done in Matlab (2005).

4. Results for one-dimensional simulations (problems I and II)

The model parameters are listed in Table 1. These values were chosen from the data available in the literature on PZT ferroelectrics in thin film and bulk form (e.g., Huber and Fleck, 2004). The creep parameters m and k were chosen to capture the correct qualitative shape of the D_3 versus E_3 hysteresis loop. The voltage loading varies linearly with time with a triangular waveform of frequency $f = 5000\dot{f}_0$. Simulations were performed for selected values of the ratio $\bar{r} = r/(1+r)$ where $r = G_c^{90}/G_c^{180}$. The values considered for $\bar{r}$ is listed in Table 2.

4.1. Effect of substrate constraint upon hysteresis loops

In this section, we explore the sensitivity of the D_3 versus E_3 hysteresis loops to the ratio $\bar{r}$ and to the presence or absence of a rigid substrate. We emphasise that the in-plane stress vanishes in the free film. In contrast, the presence of the rigid substrate enforces the in-plane biaxial strain within the film to vanish. The hysteresis loops can be characterised by the remnant polarisation P_r and by the coercive field E_c, as shown in Fig. 5. We shall make reference to these quantities in our discussion of hysteresis loops below. The remnant polarisation has particular relevance to the performance of a ferroelectric capacitor: the bistable quiescent states of then device are $D_3 = \pm P_r$ at $E_3 = 0$.

Typical hysteresis loops are shown in Fig. 6a–c for $\bar{r} = 0, 0.5$, and 1, corresponding to, respectively $r = 0, 1$, and ∞. Additionally, butterfly hysteresis loops for the in-plane stress component $\sigma_{11} = \sigma_{22} = \sigma$ versus E_3 are given in Fig. 6d for the fully constrained film. This stress is normalised by the reference stress τ_s, defined as $\tau_s = E_{180}P_0/\epsilon_0$. Before discussing the individual hysteresis loop in detail, we make a few general remarks on the predicted behaviours. The presence of substrate has little impact upon 180° switching, as this switching event does not generate a remnant strain. However, the substrate restricts 90° switching between domains

Table 1
Material parameters

Parameters	Values	Unit
Remnant polarisation (P_0)	0.5	C/m^2
Remnant strain (ϵ_0)	1%	
d_{33}	300×10^{-12}	m/V
d_{31}	-135×10^{-12}	m/V
d_{15}	525×10^{-12}	m/V
κ	5×10^{-9}	F/m
Stress exponent (m)	5.0	—
Reciprocal creep exponent (k)	1.0	—
Reference rate ($\dot{f}_0$)	2.0	s^{-1}
Shear modulus	60	GPa
Poisson's ratio	0.3	—
Number of domains (N)	6	—
Initial domain volume fraction	$1/N$	—
Switching field E_{180}	2.0	MV/m
Max. nominal field V/h	2.5 to 4 × coercive field or E_c	—
Etch angle	0°, 10°, 20°, 30°	—

Table 2
Ratios of resistance to 90° and 180° switching

$\bar{r}$	G_c^{90}	G_c^{180}
0	$2E_{180}P_0$	∞
0.5	$2E_{180}P_0/3$	$2E_{180}P_0$
0.75	$3 \times 2E_{180}P_0$	$2E_{180}P_0$
1	∞	$2E_{180}P_0$

of type 3 and 6 and those of type 1, 2, 4 and 5 (see Fig. 4 for domain types). An in-plane stress is induced by the remnant strain and by the strain associated with the change in piezoelectric tensor. According to (13) this stress restricts 90° switching. The hysteresis loops shown in Fig. 6 are for voltage cycling of fixed amplitude. The loops are cyclically stable after the first half cycle, and the hysteresis loops plotted for the first three loading cycles overlap each other. Additional cycling has been performed (up to 10 cycles) and the cyclic stability is maintained. Also, an increase in the amplitude of the voltage has a minor effect upon E_c and P_r.

Consider first the case $\bar{r} = 0$, such that only 90° switching is allowed, see Fig. 6a. The remnant polarisation P_r is sensitive to the magnitude of mechanical constraint: P_r is largest for the free-standing film and is least for the fully constrained film. For the free-standing film, switching involves all domains. When E_3 is large and positive, the ferroelectric has fully switched to the state 3 of Fig. 4. Likewise, for E_3 large and negative, the ferroelectric is in the state 6 of Fig. 4. Electrical unloading for these extreme states to $E_3 = 0$ has a negligible effect upon the remnant state and consequently $P_r = \pm P_0$. This is the maximum achievable value of polarisation for the film. For the plane strain film, switching is severely restricted in the plane strain x_2 direction, and the volume fraction of domains 2 and 5 of Fig. 4 is almost constant throughout the loading programme. These domains lie dormant and give a negligible contribution to the remnant polarisation, and so $P_r = \pm 2P_0/3$. Likewise, full constraint by the substrate enforces an almost constant volume fraction of domains 1, 2, 4 and 5 of Fig. 4, giving $P_r = \pm P_0/3$.

Second, consider the hysteresis loops in Fig. 6b for the choice $G_c^{90} = G_c^{180}$, giving $\bar{r} = 0.5$. For all three choices of constraint, the magnitude of E_c implies that the cyclic hysteresis loops are due to 180° switching: this is evident from a comparison of Fig. 6b with the simulation in Fig. 6c for 180° switching alone. However, the magnitude of polarisation is different for each level of constraint in Fig. 6b. This can be traced back to the fact that the first half cycle of electrical loading produces a different amount of 90° switching in the three cases. For the free film, initial electrical loading causes domain 6 to undergo 180° switch to variant 3. Under an increasing electric field, 90° switching of the remaining variants $(1, 2, 4, 5)$ occurs into variant 3. Consequently,

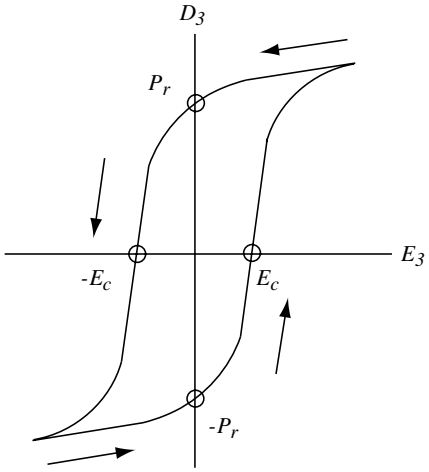

Fig. 5. Main features of a hysteresis loop.

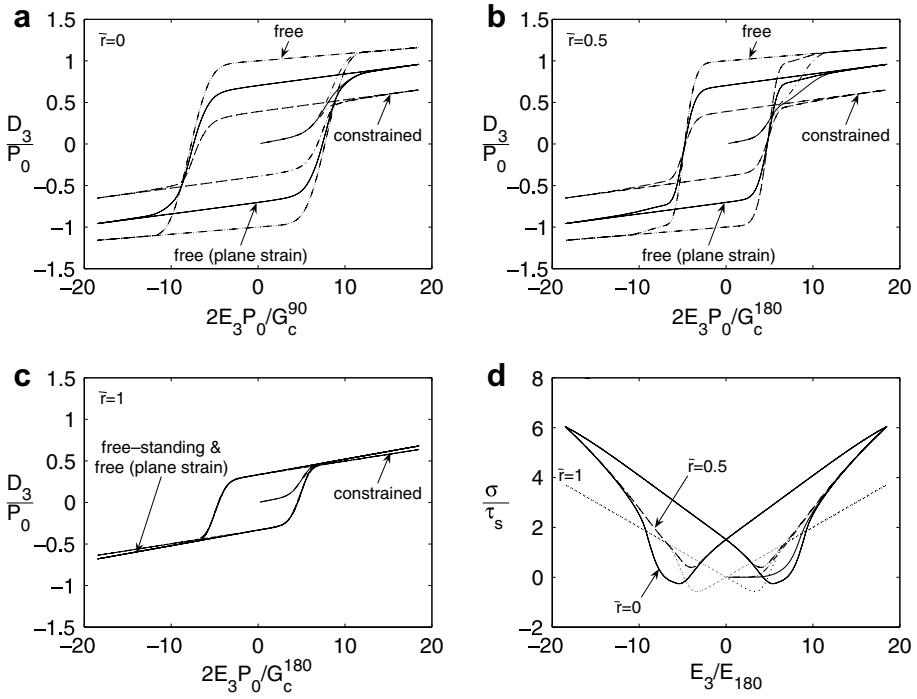

Fig. 6. Hysteresis loops of free and fully. (a) $\bar{r} = 0$, (b) $\bar{r} = 0.5$, (c) $\bar{r} = 1$ and (d) stress in fully constrained film.

the remnant polarisation achieves the maximum value $P_r = P_0$. Subsequent cyclic loading causes the fully polarised state of variant 3 to reverse by 180° switching to variant 6, and P_r drops to $-P_0$. Note that the magnitude of the required electric field for 90° switching from variant 3 to variants $(1,2,4,5)$ and from variants $(1,2,4,5)$ to variant 6 is larger than the field to drive 180° switching from variants 3 to 6.

Next, consider the response of the plane strain film and the fully constrained film at $\bar{r} = 0.5$. The presence of mechanical constraint has a negligible effect upon 180° switching but restricts 90° switching. Consequently for the film in plane strain, variants 2 and 5 undergo negligible 90° switching over the first loading half cycle and so the remnant polarisation is $2P_0/3$. Subsequent cyclic loading causes this polarisation to drop to $-2P_0/3$ and then back to $2P_0/3$, all by 180° switching. Over this history the volume fraction of variants 2 and 5 remain almost fixed. When full in-plane constraint is imposed, all four in-plane variants $(1,2,4,5)$ have almost con-

stant volume fraction, and only 180° switching can occur between variants 3 and 6. Consequently, the amplitude of P_r is $P_0/3$.

Third, consider the case of only 180° switching, $\bar{r} = 1$, as shown in Fig. 6c. Only variants 3 and 6 are involved in the switching process, and so P_r equals $\pm P_0/3$ regardless of the degree of the mechanical constraint upon the film.

Butterfly hysteresis loops of in-plane stress $\sigma_{11} = \sigma_{22} = \sigma$ versus E_3 are shown in Fig. 6d for the fully constrained film. The shapes of these loops can be interpreted as follows. (i) When the film is in a net polarised state the net piezoelectric tensor $e_{ijk} = \sum_I c_I e^I_{ijk}$ of the crystal is finite. Consequently, an in-plane stress is induced by a change in E_3, recall (8). (ii) Additionally, a change in the in-plane strain is induced by 90° switching. Such 90° switching occurs for $\bar{r} = 0$ and 0.5 by the following argument. The butterfly hysteresis loops reveal that a finite remnant strain exists at $E_3 = 0$ for the cases $\bar{r} = 0$ and 0.5. This is a consequence of the fact that upon loading to the maximum positive value of E_3, 90° switching occurs from variants $(1, 2, 4, 5)$ into variant 3 of Fig. 4. Although the volume fraction of variant 6 is zero at this extreme, the volume fraction of variant 3 is about 0.4: the 90° switching has elevated the volume fraction to above the value of 1/3, and thereby induced a finite remnant strain.

5. Results for two-dimensional simulations (problem III)

The switching response of a finite 2D ferroelectric island is explored for selected values of island aspect ratio w/h and edge inclination angle due to the etching process β, as defined in Fig. 3d. We emphasise that the island is prismatic along the plane strain x_2 direction and is thereby amenable to a 2D finite element analysis. The island is discretised by 6-noded plane strain triangular elements. Only one half of the island is needed, for $x_1 > 0$, due to symmetry. The initial state is again taken to be stress-free, with $P_r = 0$, and $c_I = 1/6$ for $I = 1$–6. The material properties are again defined in Tables 1 and 2, and a triangular waveform of voltage $\Phi(t)$ is again imposed of frequency $f = 5000\dot{f}_0$. Most simulations have been performed for the case of $\beta = 0$, corresponding to the ideal etch. Also, unless otherwise stated, the island is bonded to an elastic, insulating substrate with an identical modulus and Poisson ratio to that of the ferroelectric. The substrate is sufficiently extensive (of depth $10h$ and width $20w$) for it to behave as an elastic half-space.

The switching behaviour of the island is characterised in terms of the average surface charge density q_s on the top electrode and the voltage difference Φ between electrodes. Note that q_s plays the same role as D_3 for the free-standing and constrained films reported above. q_s is obtained by a finite element procedure as detailed at the end of Appendix B.

5.1. Typical response of a ferroelectric island

A typical prediction for the electrical performance of a ferroelectric island is shown in Fig. 7 for the choice $\bar{r} = 0.5$, $\bar{w} = w/(w + h) = 0.5$ and $\beta = 0$. The performance is contrasted with that of a plane strain film (labelled $\bar{w} = 0$) and of a fully constrained film (labelled $\bar{w} = 1$). In all three cases, the amplitude of the electric loading is fixed at $3E_c$. The remnant polarisation of the island is intermediate between those of the two films. The effect of geometry upon E_c is more minor: the island has a slightly lower value of E_c than those of the films.

It is instructive to plot the distribution of polarisation P_3 in the island. Recall that the charge on the electrodes is largely dictated by the value of P_3 adjacent to the electrodes. Contours of P_3 are shown in Fig. 8 for two values of applied voltage, states A and B of Fig. 7. State A refers to the extreme point of the hysteresis loop where the voltage Φ on the upper electrode is large and negative. State B is the point on the hysteresis loop at which the total charge on the electrodes equals zero; the average electrical field between the electrodes at this instant defines the coercive field.

The polarisation P_3 in state A (see Fig. 8a) is almost constant at $P_3 = -0.65P_0$ except near the substrate. Mechanical constraint by the substrate reduces the degree of switching and thereby the polarisation. Upon increasing the voltage on the upper electrode, switching begins and the polarisation in the ferroelectric rises. In state B, the polarisation is almost zero throughout the island (see Fig. 8b). A gradient in polarisation exists adjacent to the free side of the island. The traction-free side of the island allows switching to occur more easily and so P_3 is higher at the side of the island than in the core. A singularity in electrical displacement exists at the

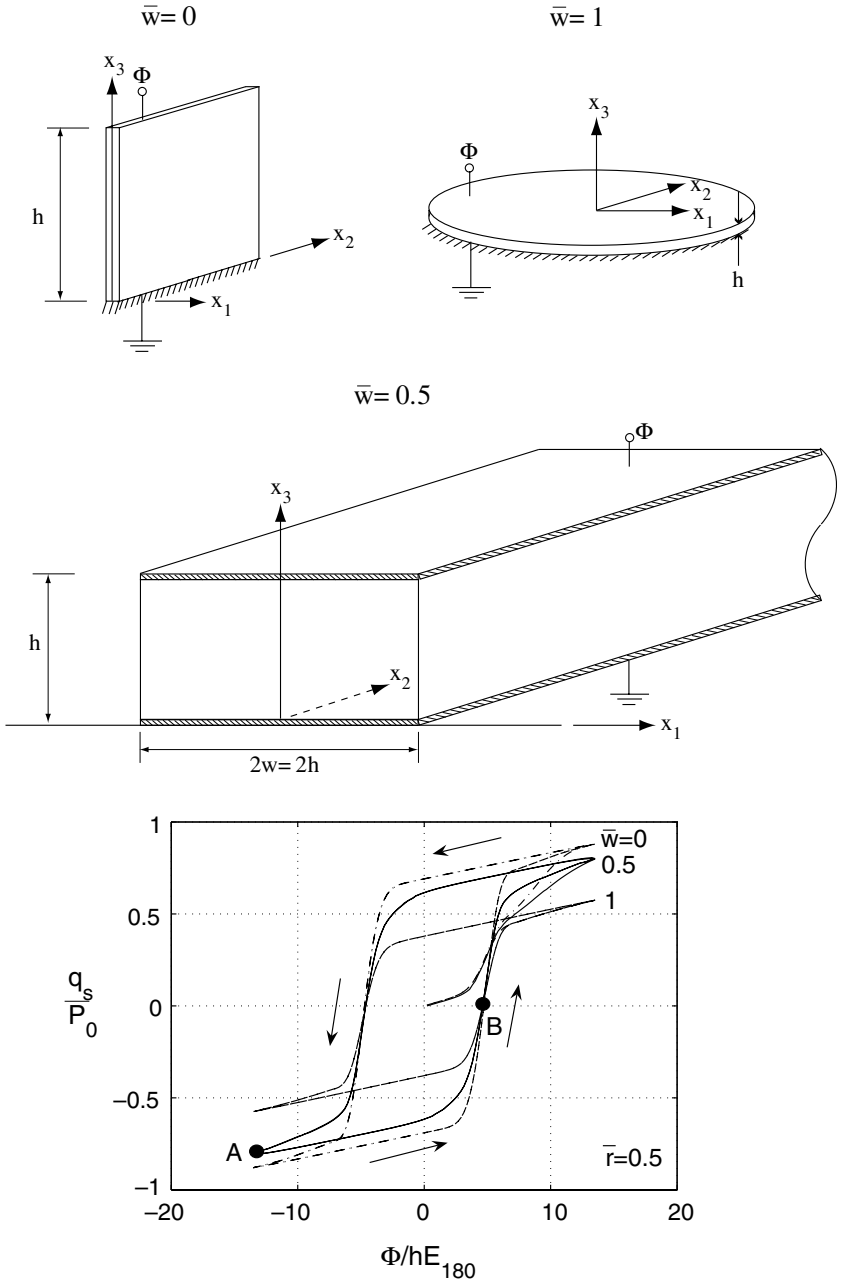

Fig. 7. Average surface charge density of a 2D island ($\bar{w} = 0.5$), a plane strain film ($\bar{w} = 0$), and a fully constrained film ($\bar{w} = 1$), $\bar{r} = 0.5$.

90° corner between the island and the substrate, but the effect of this singularity upon the overall performance is negligible. A preliminary study of singular fields at corner in piezoelectric solids has been conducted by Xu and Rajapakse (2000), but is not pursued further here.

5.2. Effect of geometry of island upon performance

The remnant polarisation P_r is a useful measure of the performance of the ferroelectric island. The dependence of P_r upon the aspect ratio $\bar{w} \equiv w/(w + h)$ is shown in Fig. 9 for selected values of $\bar{r}$ and for $\beta = 0$. The coercive field E_c is much less sensitive to $\bar{w}$ than is P_r and so the equivalent plot for E_c is omitted. The limit

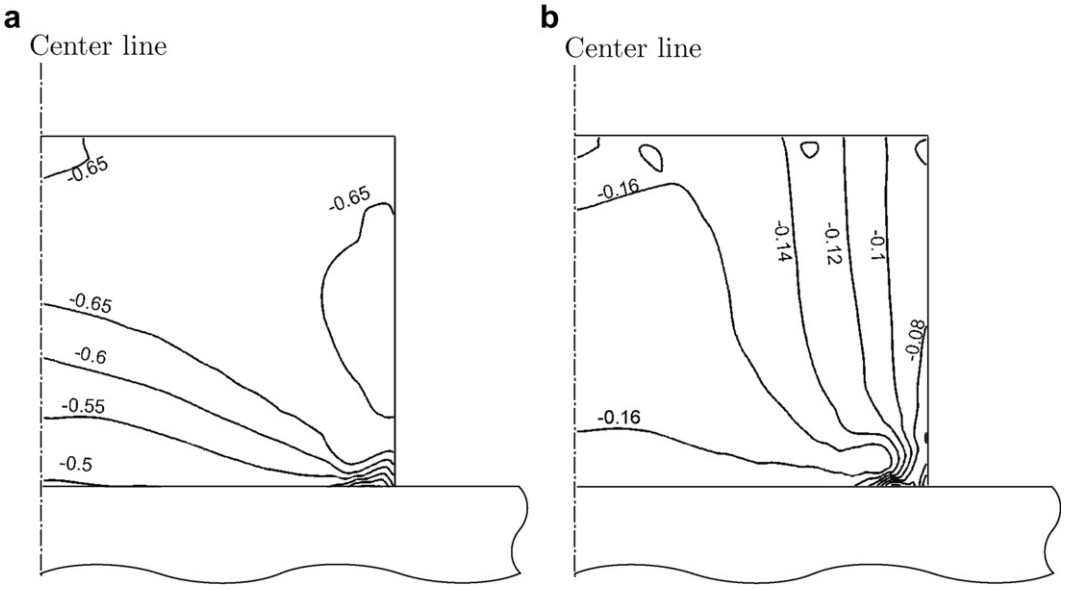

Fig. 8. Remnant polarisation in the poling direction x_3 for $\bar{w} = 0.5$ (a) state A and (b) state B.

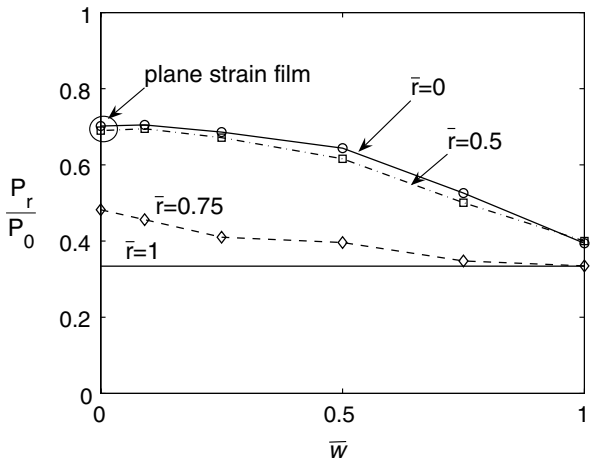

Fig. 9. Remnant polarisation P_r as a function of $\bar{w}$.

$\bar{w} = 0$ in Fig. 9 is the plane strain film while $\bar{w} = 1$ is the fully constrained film. The amplitude of the average electric field is again $3E_c$ in each case.

The switching behaviours for $\bar{w} = 0$ and 1, and for $\bar{r} = 0, 0.5$, and 1 have already been thoroughly discussed in the context of Fig. 6. The substrate constrains the ferroelectric island against 90° switching and so P_r drops with increasing $\bar{w}$. It is clear from the figure that the performance of FeRAM device is almost insensitive to the value of $\bar{r}$ provided $0 \leq \bar{r} \leq 0.5$. For this range of $\bar{r}$ and for $0 \leqslant \bar{w} \leqslant 0.5$ P_r is approximately equal to the value for the plane strain film ($\bar{w} \equiv 0$). In this parameter regime, the device performance is almost unchanged. In current design of ferroelectric capacitors $\bar{w}$ is close to unity, and so the predicted device performance is significantly below that exhibited by the plane strain film. At $\bar{r} \geqslant 0.5$, 180° switching dominates the device performance and P_r is almost insensitive to $\bar{w}$.

The effect of edge inclination angle β upon the remnant charge is now explored. The selected geometry is $\bar{w} = w_b/(w_b + h) = 0.5$, where w_b denotes the width of the bottom electrode. A series of simulations have been performed for $\bar{r} = 0, 0.5$ and 1. In each simulation the total charge of the lower electrode is calculated at $\Phi = 0$ and is denoted by Q_r. Note that the total charge on the upper electrode equals that of the lower electrode via

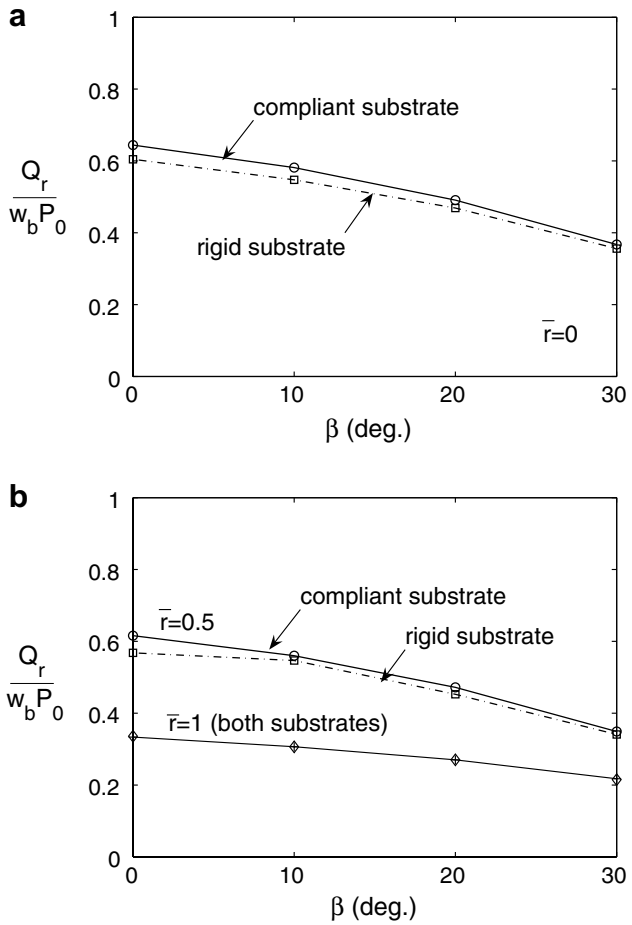

Fig. 10. Remnant polarisation P_r versus β for (a) $\bar{r} = 0$ and for (b) $\bar{r} = 0.5$ and $\bar{r} = 1$. The maximum applied field Φ/h is $3E_c$ and $\bar{w} = 0.5$.

(2). The charge is normalised by $P_0 w_b$ and plotted against β in Fig. 10. Results are given for a substrate with elastic properties identical to those of the ferroelectric, and for the case of rigid substrate.

The normalised charge $Q_r/P_0 w_b$ is a useful measure of the device performance. It is similar to the remnant polarisation of the device P_r of Fig. 5 measured at the lower electrode. We note that for all $\bar{r}$ considered, $Q_r/P_0 w_b$ drops with increasing β. Also, $Q_r/P_0 w_b$ is slightly less for a rigid substrate than for a compliant substrate provided that 90° switching is allowed (i.e. $\bar{r} = 0$ and 0.5). This figure gives a quantitative prediction for the sensitivity of device performance to the etch angle β. We conclude that it is best to make β as small as possible by a suitable choice of processing conditions.

6. Concluding remarks

The influence of geometrical and switching parameters upon the performance of a ferroelectric memory element has been explored. The extent of substrate clamping, the geometry of FeRAM device, and the relative ease of 90° versus 180° switching each affects the device performance, as measured by the surface charge density in the poled state.

Mechanical constraint by a substrate reduces the achievable polarisation in a FeRAM device when 90° switching is the dominant switching event. In contrast, 180° switching is less influenced by the presence or absence of a substrate.

This study suggests that the performance of a FeRAM device is influenced by the aspect ratio (w/h) and the etch angle β. A reduction in w/h relaxes the substrate constraint and leads to greater polarisation, and hence to

improved performance in terms of charge storage per unit area. A reduction of the etch angle β also improves performance. In practical devices, process limitations dictate the minimum aspect ratio and the squareness of etch that can be achieved; our analysis predicts that gains in performance are achievable through improvements in processing technique.

Appendix A. Rate tangent formulation

A.1. Derivation

Recall from (14) that the rate of volume fraction change due to the αth transformation system is given by

$$\dot{f}^{\alpha} = \dot{f}_0 \left| \frac{G^{\alpha}}{G_c^{\alpha}} \right|^{m-1} \frac{G^{\alpha}}{G_c^{\alpha}} \left(\frac{c_I}{c_0} \right)^{1/k} \tag{A-1}$$

Define the increment of volume fraction of the transformation system α at time $n+\theta$ as:

$$\Delta f^{\alpha} = \Delta t[(1-\theta)\dot{f}_n^{\alpha} + \theta \dot{f}_{n+1}^{\alpha}] \tag{A-2}$$

where θ is a chosen parameter between 0 and 1. The choice $\theta = 0$ corresponds to the forward Euler method and $\theta = 1$ to the backward Euler method. Write:

$$\dot{f}_{n+1}^{\alpha} = \dot{f}_n^{\alpha} + \frac{\partial \dot{f}^{\alpha}}{\partial G^{\alpha}} \Delta G^{\alpha} + \frac{\partial \dot{f}^{\alpha}}{\partial c^I} \Delta c^I \tag{A- 3}$$

$$\chi^{\alpha} \equiv \frac{\partial \dot{f}^{\alpha}}{\partial G^{\alpha}} = \frac{m \dot{f}_0}{G_c^{\alpha}} \left(\frac{G^{\alpha}}{G_c^{\alpha}} \right)^{m-1} \left(\frac{c_I}{c_0} \right)^{1/k} \tag{A- 4}$$

$$\lambda^{\alpha} \equiv \frac{\partial \dot{f}^{\alpha}}{\partial c^I} = \frac{\dot{f}_0}{k c_0} \left(\frac{G^{\alpha}}{G_c^{\alpha}} \right)^{m} \left(\frac{c_I}{c_0} \right)^{1/k-1} \tag{A-5}$$

where $\Delta G^{\alpha} = \Delta t \dot{G}^{\alpha}$ and $\Delta c^{\alpha} = \sum_{\beta} I^{\alpha\beta} \Delta f^{\beta}$. The matrix $I^{\alpha\beta}$ is a Boolean matrix (contains 0, 1 and -1) that accounts for the contribution of all transformation systems β to the volume fraction of the domain involved in the transformation system α.

The driving force for the αth transformation can be written as:

$$G^{\alpha} = \sigma_{ij} \left(\mu_{ij}^{\alpha} \Delta \gamma^{\alpha} + \frac{1}{2} \tilde{\epsilon}_{ij}^{\alpha} \right) + E_i \left(s_i^{\alpha} \Delta P^{\alpha} + \frac{1}{2} \tilde{D}_i^{\alpha} \right) \tag{A-6}$$

where

$$\tilde{\epsilon}_{ij}^{\alpha} = \Delta s_{ijkl}^{E\alpha} \sigma_{kl} + \Delta d_{kij}^{\alpha} E_k \widetilde{D}_i^{\alpha} = \Delta d_{ikl}^{\alpha} \sigma_{kl} + \Delta \kappa_{ik}^{\sigma\alpha} E_k \tag{A-7}$$

The rate of this driving force is

$$\dot{G}^{\alpha} = \dot{\sigma}_{ij} \hat{\epsilon}_{ij}^{\alpha} + \dot{E}_i \widehat{D}_i^{\alpha} \tag{A-8}$$

where $\hat{\epsilon}_{ij}^{\alpha} = \tilde{\epsilon}_{ij}^{\alpha} + \mu_{ij}^{\alpha} \Delta \gamma^{\alpha}$ and $\widehat{D}_i^{\alpha} = \widetilde{D}_i^{\alpha} + s_i^{\alpha} \Delta P^{\alpha}$. Now, (A-3) can be expressed as:

$$\dot{f}_{n+1}^{\alpha} = \dot{f}_n^{\alpha} + \Delta t \left\{ \chi^{\alpha} \left(\dot{\sigma}_{ij} \hat{\epsilon}_{ij}^{\alpha} + \dot{E}_i \widehat{D}_i^{\alpha} \right) + \lambda^{\alpha} \sum_{\beta} I^{\alpha\beta} \dot{f}^{\beta} \right\} \tag{A-9}$$

and (A-2) becomes,

$$\frac{\Delta f^{\alpha}}{\Delta t} = \dot{f}_{n+\theta}^{\alpha} = \dot{f}_n^{\alpha} + \theta \Delta t \left\{ \chi^{\alpha} (\dot{\sigma}_{ij} \hat{\epsilon}_{ij}^{\alpha} + \dot{E}_i \widehat{D}_i^{\alpha}) + \lambda^{\alpha} \sum_{\beta} I^{\alpha\beta} \dot{f}^{\beta} \right\} \tag{A-10}$$

The rates of stress and electric displacement from (11) and (12) become

$$\begin{aligned} \dot{\sigma}_{ij} &= c_{ijkl} \left(\dot{\epsilon}_{kl} - \sum_{\alpha} \dot{f}_{n+\theta}^{\alpha} \hat{\epsilon}_{kl}^{\alpha} \right) - e_{kij} \dot{E}_k \\ \dot{D}_i &= e_{ikl} \dot{\epsilon}_{kl} + \kappa_{ik}^{\epsilon} \dot{E}_k + \sum_{\alpha} \dot{f}_{n+\theta}^{\alpha} (\widehat{D}_i^{\alpha} - d_{ikl} \bar{\sigma}_{kl}^{\alpha}) = e_{ikl} \left(\dot{\epsilon}_{kl} - \sum_{\alpha} \dot{f}_{n+\theta}^{\alpha} \hat{\epsilon}_{kl}^{\alpha} \right) + \sum_{\alpha} \dot{f}_{n+\theta}^{\alpha} \widehat{D}_i^{\alpha} \end{aligned} \tag{A-11}$$

where $e_{ijk} = c_{ijmn}d_{kmn}$, $\bar{\sigma}^{\alpha}_{ij} = c_{ijkl}\hat{\epsilon}^{\alpha}_{kl}$ and $\kappa^{\epsilon}_{ik} = \kappa^{\sigma}_{ik} - d_{irs}c_{pqrs}d_{kpq}$. Substituting (A-11) into (A-10) gives,

$$\dot{f}^{\alpha}_{n+\theta} = \dot{f}^{\alpha}_{n} + \theta\Delta t\left\{A^{\alpha}_{ij}\dot{\epsilon}_{ij} + B^{\alpha}_{i}\dot{E}_{i} + \sum_{\beta} M^{\alpha\beta}\dot{f}^{\beta}_{n+\theta}\right\} \tag{A-12}$$

where

$$\begin{aligned} A^{\alpha}_{ij} &= \chi^{\alpha}c_{ijkl}\hat{\epsilon}^{\alpha}_{kl} \\ B^{\alpha}_{i} &= \chi^{\alpha}\left(\widehat{D}^{\alpha}_{i} - e_{ikl}\hat{\epsilon}^{\alpha}_{kl}\right) \\ M^{\alpha\beta} &= \lambda^{\alpha}I^{\alpha\beta} - \chi^{\alpha}\hat{\epsilon}^{\alpha}_{ij}c_{ijkl}\hat{\epsilon}^{\beta}_{kl} \end{aligned} \tag{A-13}$$

To solve for $\dot{f}^{\alpha}_{n+\theta}$, (A-12) is rearranged into the form,

$$\dot{f}^{\alpha}_{n+\theta} = \sum_{\beta} N^{\alpha\beta}\{\dot{f}^{\beta}_{n} + \theta\Delta t(A^{\beta}_{ij}\dot{\epsilon}_{ij} + B^{\beta}_{i}\dot{E}_{i})\} \tag{A-14}$$

where $N^{\alpha\beta} = [\delta^{\alpha\beta} - \theta\Delta t M^{\alpha\beta}]^{-1}$.

A.2. Tangent moduli

Recall from (18) that the principle of virtual work in rate form is:

$$\int_{V}[\dot{\sigma}_{ij}\delta\epsilon_{ij} + \dot{D}_{i}\delta E_{i}]\mathrm{d}V = \int_{S}[\dot{t}_{i}\delta u_{i} - \dot{Q}\delta\phi]\mathrm{d}S + \int_{V}[\dot{f}_{i}\delta u_{i} + \dot{q}\delta\phi]\mathrm{d}V \tag{A-15}$$

To find the tangent moduli, (A-14) is substituted into (A-11) to obtain:

$$\begin{aligned} \dot{\sigma}_{ij} &= c^{\tan}_{ijkl}\dot{\epsilon}_{kl} - e^{\tan}_{kij}\dot{E}_{k} - \dot{r}^{\sigma}_{ij} \\ \dot{D}_{i} &= e^{\tan}_{ikl}\dot{\epsilon}_{kl} + \kappa^{\tan}_{ik}\dot{E}_{k} + \dot{r}^{D}_{i} \end{aligned} \tag{A-16}$$

where the tangent modulus tensor $c^{\tan}_{ijkl}$, the tangent coupled tensor $e^{\tan}_{ijk}$, and the tangent dielectric tensor $\kappa^{\tan}_{ij}$ are given by:

$$\begin{aligned} c^{\tan}_{ijkl} &= c_{ijkl} - \theta\Delta t\sum_{\alpha}\sum_{\beta}N^{\alpha\beta}A^{\alpha}_{ij}A^{\beta}_{kl}/\chi^{\alpha} \\ e^{\tan}_{ijk} &= e_{ijk} + \theta\Delta t\sum_{\alpha}\sum_{\beta}N^{\alpha\beta}A^{\alpha}_{ij}B^{\beta}_{k}/\chi^{\alpha} \\ \kappa^{\tan}_{ij} &= \kappa^{\epsilon}_{ij} + \theta\Delta t\sum_{\alpha}\sum_{\beta}N^{\alpha\beta}B^{\alpha}_{i}B^{\beta}_{j}/\chi^{\alpha} \end{aligned} \tag{A-17}$$

The form (A-16) includes the internal mechanical and electrical body forces

$$\begin{aligned} \dot{r}^{\sigma}_{ij} &= \sum_{\alpha}\sum_{\beta}N^{\alpha\beta}\dot{f}^{\beta}_{n}A^{\alpha}_{ij}/\chi^{\alpha} \\ \dot{r}^{D}_{i} &= \sum_{\alpha}\sum_{\beta}N^{\alpha\beta}\dot{f}^{\beta}_{n}B^{\alpha}_{i}/\chi^{\alpha} \end{aligned} \tag{A-18}$$

Substituting (A-16) and (A-17) into (A-15) gives the rate tangent form of the FE equation with internal body forces due to (A-18). The finite element method is used to solve (A-15) in order to obtain $\dot{\epsilon}_{ij}$ and $\dot{E}_{i}$.

In the finite element computation reported herein we have simplified the implementation of the rate tangent method by ignoring the term involving λ^{α} in (A-13). The rate tangent method gives a much improved convergence rate than the simpler forward Euler method.

Appendix B. Finite element implementation

The rate form (19) of the virtual work expression is discretised using a plane strain six-node triangular element. Each node has two displacement degree of freedoms $\mathbf{u}^{n}$ and one potential degree of freedom ϕ^{n}. Shape functions $N^{n}(\mathbf{x})$ and $L^{n}(\mathbf{x})$ are introduced for the displacement $\mathbf{u}$ and the electric potential ϕ, respectively, as:

$$\mathbf{u} = \sum_n N^n(\mathbf{x})\mathbf{u}^n \tag{B-1}$$

$$\phi = \sum_n L^n(\mathbf{x})\phi^n \tag{B-2}$$

Unless otherwise stated the summation is from $n = 1$ to 6. The usual strain–displacement relation $\epsilon_{ij} = (u_{i,j} + u_{j,i})/2$ and the electric field relation (3) $E_i = -\phi_{,i}$ are used to obtain:

$$\epsilon_{ij} = \sum_n B^n_{ij}(\mathbf{x})\mathbf{u}^n \tag{B-3}$$

$$E_i = -\sum_n \Theta^n_i(\mathbf{x})\phi^n \tag{B-4}$$

Now substitute (B-1)–(B-4) into (19) to obtain,

$$\Delta t \sum_n \int_V [\dot{\sigma}_{ij} B^n_{ij}\delta\mathbf{u}^n + \dot{D}_i\Theta^n_i\delta\phi^n]\mathrm{d}V = \Delta t \sum_n \int_S [\dot{\mathbf{t}}N^n\delta\mathbf{u}^n + \dot{Q}L^n\delta\phi^n]\mathrm{d}S$$
$$+ \sum_n \left\{ \int_S [\mathbf{t}N^n\delta\mathbf{u}^n + QL^n\delta\phi^n]\mathrm{d}S - \int_V [\sigma_{ij}B^n_{ij}\delta\mathbf{u}^n + D_i\Theta^n_i\delta\phi^n]\mathrm{d}V \right\} \tag{B-5}$$

Make use of (A-16) together with (A-17) and (A-18), for the stress rate and electric displacement rate. At the element level, virtual work now reads

$$\Delta t \begin{pmatrix} \mathbf{k}^{\tan}_{BB} & \mathbf{k}^{\tan}_{B\Theta} \\ \mathbf{k}^{\tan}_{\Theta B} & \mathbf{k}^{\tan}_{\Theta\Theta} \end{pmatrix} \begin{pmatrix} \dot{\mathbf{u}} \\ \dot{\phi} \end{pmatrix} = \Delta t \begin{pmatrix} \dot{\mathbf{f}}^B \\ \dot{\mathbf{f}}^\Theta \end{pmatrix} + \begin{pmatrix} \mathbf{f}^B_{\mathrm{corr}} \\ \mathbf{f}^\Theta_{\mathrm{corr}} \end{pmatrix} \tag{B-6}$$

where

$$\begin{pmatrix} \mathbf{k}^{\tan}_{BB} & \mathbf{k}^{\tan}_{B\Theta} \\ \mathbf{k}^{\tan}_{\Theta B} & \mathbf{k}^{\tan}_{\Theta\Theta} \end{pmatrix} = \sum_m \sum_n \int_V \begin{pmatrix} B^m_{ij} c^{\tan}_{ijkl} B^n_{kl} & B^m_{ij} e^{\tan}_{ijk} \Theta^n_k \\ -\Theta^m_i e^{\tan}_{ijk} B^n_{jk} & \Theta^m_i \kappa^{\tan}_{ij} \Theta^n_j \end{pmatrix} \mathrm{d}V \tag{B-7}$$

and

$$\begin{pmatrix} \dot{\mathbf{f}}^B \\ \dot{\mathbf{f}}^\Theta \end{pmatrix} = \sum_n \int_S \begin{pmatrix} \dot{\mathbf{t}}N^n + \dot{r}^\sigma_{ij} B^n_{ij} \\ \dot{Q}L^n - \dot{r}^D_i \Theta^n_i \end{pmatrix} \mathrm{d}S \tag{B-8}$$

and

$$\begin{pmatrix} \mathbf{f}^B_{\mathrm{corr}} \\ \mathbf{f}^\Theta_{\mathrm{corr}} \end{pmatrix} = \sum_n \int_S \begin{pmatrix} \mathbf{t}N^n \\ QL^n \end{pmatrix} \mathrm{d}S - \sum_n \int_V \begin{pmatrix} \sigma_{ij} B^n_{ij} \\ D_i \Theta^n_i \end{pmatrix} \mathrm{d}V \tag{B-9}$$

A global stiffness matrix and force vector are assembled over all elements, and the resulting system of linear equations in $(\dot{\mathbf{u}}^n, \dot{\phi}^n)$ are solved.

B.1. Calculation of q_s

The average surface charge density q_s on the bottom electrode is obtained from the finite element solution as follows. The principle of virtual work (18) is rewritten in the finite element form analogous to (B-5),

$$\sum_n \int_V [\sigma_{ij} B^n_{ij}\delta\mathbf{u}^n + D_i\Theta^n_i\delta\phi^n]\mathrm{d}V = \sum_n \int_S [\mathbf{t}N^n\delta\mathbf{u}^n + QL^n\delta\phi^n]\mathrm{d}S \tag{B-10}$$

Now make the choice of virtual nodal quantities, $\delta\mathbf{u}^n \equiv 0$ and $\delta\phi^n = \phi^n$ to obtain:

$$q_s \times S_e = \sum_n \int_V D_i\Theta^n_i\delta\phi^n\mathrm{d}V \tag{B-11}$$

where S_e is the surface area of the bottom electrode. The prescription (B-11) is used to evaluate q_s.

References

Abaqus 6.5, ABAQUS, Inc., Rhode Island, USA.

Alexe, M., Harnagea, C., Hesse, D., Gosele, U., 2001. Polarization imprint and size effects in mesoscopic ferroelectric structures. Appl. Phys. Lett. 79, 242–244.

Alexe, M., Harnagea, C., Erfurth, W., Hesse, D., Gosele, U., 2000. 100 nm lateral size ferroelectric memory cells fabricated by electron-beam direct writing. Appl. Phys. A 70, 247–251.

Alik, H., Hughes, T.J.R., 1970. Finite element method for piezoelectric vibration. Int. J. Numer. Methods Eng. 2, 151–157.

Chu, D.P., 2004. Ferroelectric random access memory (FeRAMS) cells and non-destructive read-out (NDRO). In: Proceedings of 3rd ECS International Semiconductor Technology Conference (ISTC), 94–99.

Dawber, M., Rabe, K.M., Scott, J.F., 2005. Physics of thin-film ferroelectric oxides. Rev. Mod. Phys. 77, 1083–1130.

Gong, X., Suo, Z., 1996. Reliability of ceramic multilayer actuators: a nonlinear finite element simulation. J. Mech. Phys. Solids 44 (5), 751–769.

Haug, A., Huber, J.E., Onck, P.R., Van der Giessen, E., 2007. Multi-grain analysis versus self-consistent estimates of ferroelectric polycrystals. J. Mech. Phys. Solids 55 (3), 648–665.

Huber, J.E., Fleck, N.A., Landis, C.M., McMeeking, R.M., 1999. A constitutive model for ferroelectric polycrystals. J. Mech. Phys. Solids 47 (8), 1663–1697.

Huber, J.E., Fleck, N.A., 2001. Multi-axial electrical switching of a ferroelectric: theory versus experiment. J. Mech. Phys. Solids 49 (4), 785–811.

Huber, J.E., Fleck, N.A., 2004. Ferroelectric switching: a micromechanics model versus measured behavior. Eur. J. Mech. A 23, 203–217.

Jaffe, B., Roth, R.S., Marzullo, S., 1954. J. Appl. Phys. 25, 809.

Jaffe, B., Cook Jr., W.R., Jaffe, H., 1971. Piezoelectric Ceramics. Academic Press, London.

Jung, D.J., Morrison, F.D., Dawber, M., Kim, H.H., Kim, K., Scott, J.F., 2004. Effect of microgeometry on switching and transport in lead zirconate titanate capacitors: implications for etching of nano-ferroelectrics. J. Appl. Phys. 95 (9), 4968–4975.

Kessler, H., Balke, H., 2001. On the local and average energy release in polarization switching phenomena. J. Mech. Phys. Solids 49 (5), 953–978.

Kim, K.T., Song, S.H., Kim, C.I., 2004. Effect of thickness on ferroelectric properties of $Bi_{3.25}La_{0.75}Ti_3O_{12}$ thin films on $Pt/Ti/SiO_2/Si$ substrates. J. Vac. Sci. Tech. A 22 (4), 1315–1318.

Li, Y.L., Hu, S.Y., Liu, Z.K., Chen, L.Q., 2001. Phase-field model of domain structures in ferroelectric thin films. Appl. Phys. Lett. 78 (24), 3878–3880.

Li, Y.L., Hu, S.Y., Liu, Z.K., Chen, L.Q., 2002. Effect of substrate constraint on the stability and evolution of ferroelectric domain structures in thin films. Acta Mater. 50 (2), 395–411.

Loge, R.E., Suo, Z., 1996. Nonequilibrium thermodynamics of ferroelectric domain evolution. Acta Mater. 44, 3429–3438.

Matlab 7.7, The MathWorks, Massachusetts, USA.

Miller, S.L., Nasby, R.D., Schwank, J.R., Rodgers, M.S., Dressendorfer, P.V., 1990. Device modeling of ferroelectric capacitors. J. Appl. Phys. 68 (12), 6463–6471.

Needleman, A., Asaro, R.J., Lemonds, J., Peirce, D., 1985. Finite element analysis of crystalline solids. Comput. Methods Appl. Mech. Eng. 52 (1-3), 689–708.

Paruch, P., Giamarchi, T., Triscone, J.M., 2005. Domain wall roughness in epitaxial ferroelectric $PbZr_{0.2}Ti_{0.8}O_3$ thin films. Phys. Rev. Lett. 94, 197601.

Peirce, D., Asaro, R.J., Needleman, A., 1983. Material rate dependence and localized deformation in crystalline solids. Acta Mater. 31 (12), 1951–1976.

Pintilie, L., Gomes, M.J.M., Zhao, T., Ramesh, R., Alexe, M., 2005. Metal-ferroelectric-metal heterostructures with Schottky contacts. I. Influence of the ferroelectric properties. J. Appl. Phys. 98, 1241031–1241038.

Pintilie, L., Alexe, M., 2005. Metal-ferroelectric-metal heterostructures with Schottky contacts. II. Analysis of the experimental current-voltage and capacitance-voltage characteristics of Pb(Zr,Ti)O3 thin films. J. Appl. Phys. 98, 1241041–1241049.

Scott, J.F., Morrison, F.D., Miyake, M., Zubko, P., Lou, X.J., Kugler, V.M., Rios, S., Zhang, M., Tatsuta, T., Tsuji, O., Leedham, T.J., 2005. Recent materials characterizations of 2D and 3D thin film ferroelectric structures. J. Am. Ceram. Soc. 88 (7), 1691–1701.

Shirane, G., Hoshino, S., 1951. J. Phys. Soc. Jpn. 6, 265.

Sreenivas, K., Sayer, M., 1988. Characterization of $Pb(Zr,Ti)O_3$ thin films deposited from multielement metal targets. J. Appl. Phys. 64 (3), 1484–1493.

Tang, X.G., Jiang, L.L., Ding, A.L., 2003. The effect of thickness on the dielectric properties of highly (111) oriented $Pb(Zr0.53Ti0.47)O_3$ thin films prepared by a simple sol–gel route. Microelectron. Eng. 65 (4), 387–393.

Tybell, T., Paruch, P., Giamarchi, T., Triscone, J.M., 2002. Domain wall creep in Epitaxial ferroelectric $Pb(Zr_{0.2}Ti_{0.8})O_3$ thin films. Phys. Rev. Lett. 89 (9), 097601.

Xu, X.L., Rajapakse, R.K.N.D., 2000. On singularities in composite piezoelectric wedges and junctions. Int. J. Solids Struct. 37 (23), 3253–3275.

Yi, G., Wu, Z., Sayer, M., 1988. Preparation of $Pb(Zr,Ti)O_3$ thin films by sol gel processing: electrical, optical, and electro-optic properties. J. Appl. Phys. 64 (5), 2717–2724.

Zhang, W., Bhattacharya, K., 2005. A computational model of ferroelectric domains. Part II: grain boundaries and defect pinning. Acta Mater. 53 (1), 199–209.